Mapping Geothermal Heat Flux Using Permafrost Thickness Constrained by Airborne ElectroMagnetic Surveys on the Western Coast of Ross Island, Antarctica

Neil Foley[1], Slawomir Tulaczyk[1], Esben Auken[2], Denys Grombacher[2], Jill Mikucki[3], Nikolaj Foged[2], Krista Myers[4], Hilary Dugan[5], Peter Doran[4], Ross Virginia[6]

[1]UC Santa Cruz, [2]University of Aarhus, [3]University of Tennessee – Knoxville, [4]Louisiana State University, [5]University of Wisconsin – Madison, [6]Dartmouth College

Corresponding Author:
Neil Foley
UC Santa Cruz Department of Earth and Planetary Science
1156 High St, Santa Cruz, California, USA, 95064
781-879-2127
ntfoley@ucsc.edu

Left Running Heading: Foley, Tulaczyk, Auken, Mikucki, Foged, Myers, Dugan, Doran, Virginia

Right Running Heading: Geothermal heat flux from electrical resistivity
DateStamp: Submitted 9/30/18

ABSTRACT

Permafrost is ubiquitous at high latitudes, and its thickness is controlled by important local factors like geothermal flux, ground surface temperature, and thermal properties of the subsurface. We use airborne transient electromagnetic resistivity measurements to determine permafrost thickness on the coast of Ross Island, Antarctica, which contains the active volcano Mt Erebus. Here, resistivity data clearly distinguishes resistive permafrost from the electrically conductive fluid-saturated materials underlying it. For our study, we define permafrost as frozen material with a resistivity >100 Ω-m; more conductive material contains a significant fraction of water or (more likely) brine. We observe that permafrost is very thin near the coast and thickens within several hundred meters inland to reach depths that are typically within the range of 300-400 m. We attribute the sharp near-shore increase of permafrost thickness to lateral heat conduction from the relatively warm ocean, possibly combined with seawater infiltration into the near-shore permafrost. We validate this result with a two-dimensional heat flow model and conclude that away from the thermal influence of the ocean, the local geothermal gradient and heat flux are about 45 ±5 °C /km and 90 mW/m^2 ±13 mW/m^2, respectively. These values are in line with published estimates in the vicinity of Mount Erebus and within the actively extending Terror Rift, but do not reflect a strong heat flow anomaly from volcanic activity of Mt Erebus. Measurements made previously in the McMurdo Dry Valleys, on the other side of McMurdo Sound, tend to be a few dozens of mW/m^2 lower, likely reflecting its different tectonic setting on the uplifted rift shoulder of Transantarctic Mountains. Our study demonstrates a new approach towards constraining geothermal flux in polar regions using AEM data that can be relatively efficiently collected on regional scales where ice coverage does not exceed the penetration limits of the AEM device, which for the device used is about 500m under the favorable conditions in the study area.

Key Words: geothermal flux, electrical resistivity, Antarctica, permafrost,.

INTRODUCTION

Geothermal heat flux (GHF) is a key constraint on Earth's crustal and near-surface evolution and history (Davies and Davies, 2010). It plays a particularly significant role in high polar environments where it helps to control the thickness of permafrost, distribution of groundwater, and motion of glaciers and ice sheets (Lachenbruch et al., 1982; McKenzie and Voss, 2013; Fisher et al., 2015; Begeman et al., 2017). Geothermal energy resources in high polar environments may play an increasing role in meeting future human energy needs (Ragnarsson, 2003), including its increasing utilization in support of polar research facilities (e.g., Kyle, 1990), although significant barriers to practical implementation at high latitude remain.

Despite the scientific and practical importance of constraining GHF in polar regions, obtaining measurements and estimates of this quantity is challenging due to the technical difficulty and logistical barriers associated with drilling through permafrost and glacier ice in remote polar environments (e.g., Melles et al., 2011; Tulaczyk et al., 2014). Furthermore, it is increasingly recognized that polar environments need to be protected because they may contain uniquely adapted organisms and habitats subject to limited human disturbance (e.g., Doran and Vincent, 2011). Such environmental protection measurements increase the difficulty of borehole drilling and temperature gradient measurements in sensitive polar regions (Tulaczyk et al., 2015).

Here we present a geophysical approach towards mapping geothermal heat flux in a high polar environment using an Airborne ElectroMagnetics (AEM) survey of permafrost thickness at the western flank of the Mount Erebus volcano, Antarctica (Figure 1). This survey, which covered about 20km^2, was part of a larger 2011 campaign in the McMurdo Dry Valleys region which collected time domain EM data over 300 km^2 in total. Time domain EM methods are ideal interrogating the first several hundred meters of the subsurface while being small and light enough for an airborne package. The first such survey to use them in Antarctica (2011) detected liquid brines beneath glaciers and permafrost (Mikucki et al., 2015; Foley et al., 2015) and various lakes (Mikucki et al., 2015; Dugan et al., 2015) in the Dry Valleys. A 2018 follow up survey using an improved system found evidence of sub-permafrost submarine groundwater discharge (Foley et al., 2019) across a similar area.

Various other electrical techniques have been used in Antarctica across a variety of scales and regions. Direct current methods, which require physical and electrical contact with the surface, have been used to study the Antarctic ice sheets (e.g., Hochstein, 1967), ice shelves (e.g., Bentley, 1977) and on frozen ground in the Dry Valleys (McGinnis et al., 1973). Frequency domain methods, an electromagnetic technique closely related to time domain electromagnetics, have been used before in Antarctica on both ground-based and airborne platforms, including to detect brine beneath permafrost (Ruotoistenmäki and Lehtimäki, 1997). Frequency domain EM is often used to measure Antarctic sea ice thickness (e.g., Worby *et al.*, 1999), including on helicopter borne packages (Rack et al., 2013). In the Arctic, helicopter borne systems are commonly used to measure sea ice with great accuracy (Pfaffling et al., 2007). Northern hemisphere permafrost is also measured with a variety of electromagnetic techniques (Hauck et al., 2001; Todd and Dallimore, 2002; Korhonen et al.,

2009). Magnetotellurics, with their ability to image to great depth, have been used to investigate the magmatic system of Mt Erebus (Hill et al., 2017), the state of the bottom of the ice sheet through the lithosphere at the South Pole (Wannamaker et al., 2004) and the Transantarctic Mountains (Wannamaker et el., 2017).

This survey, a subset of the 2011 AEM campaign, covered the western coastal zone of Ross Island stretching from Cape Evans in the south to near (but not into) the edges of the Antarctic Specially Protected Areas ('ASPA') on Cape Royds in the North, and reached from a few hundred meters to a few kilometers inland. Permafrost is readily detectable in the AEM data because it represents a high-resistivity frozen layer underlain by a lower resistivity, fluid-saturated medium. For clarity, we use the term 'permafrost layer' to refer to the upper part of the subsurface in which solid ice exists in some or all interstitial space. By assuming that the permafrost is in steady-state and estimating its surface and bottom temperatures, we calculate the conductive temperature gradient through the permafrost layer and estimate GHF. Our GHF values fall around 100 mW m^{-2} which is close to the middle of the GHF range reported previously for this region (Morin et al., 2010) and is consistent with our study area being on the flank of an active volcano (Parmelee et al., 2015) where surface volcanic rocks date to 70-90,000 years ago (Harpel et al., 2004).

METHODS

Airborne EM Resistivity

In late 2011 we measured subsurface electrical resistivity across the McMurdo Sound region (Mikucki et al., 2015) using a helicopter-borne time-domain electromagnetic (TEM) sensor, commercially known as SkyTEM (Sørensen and Auken, 2004). The SkyTEM system has a rigid frame approximately 20 m by 30 m in dimension on which a transmitter coil, TEM instrumentation, and receiver coil are mounted. The frame is suspended beneath a helicopter and measurements are conducted as the helicopter flies. The system used in this survey has a maximum transmitter moment of approximately 160,000 Am^2 and uses a dual moment transmitter that is capable of recording near-surface (10s of meters) resistivity with the low moment, and deep (100s of meters) resistivity with the high moment. Dual moment acquisition balances high-resolution in the near-surface with large penetration depths; low and high-moments in this case refer to signals collected following a current pulse of 9.5 A and 95 A, respectively. The TEM signal is produced by pulsing a current in the transmitter coil, which is shut off as rapidly as possible. During the current turn-off, a time-varying magnetic field is induced in the subsurface. This time-varying magnetic field generates eddy-currents in the subsurface, which in turn generate a secondary time-varying magnetic field that can be detected inductively using a receiver coil mounted on the suspended frame. The amplitude and time-characteristics of the observed time-varying secondary field contain information about the electrical resistivity structure of the subsurface. Electrical properties of the Earth can be used to gain insight into subsurface geology; for example, permafrost regions have large resistivities while regions containing unfrozen brines have very low resistivities. Readers are directed to chapter 6 of Kirsch (2009) for a more comprehensive discussion of the TEM method. An alternative airborne EM method that has been previously employed at high-latitudes is frequency-domain electromagnetics (FEM) (Kovacs and Holladay, 1990; Multata et al., 1996; Haas et al., 2009; Ball et al., 2011; Minsley et al., 2012). TEM and FEM differ in data acquisition protocol, where FEM measurements continuously oscillate currents and measure signals while currents are still present in the transmitter coil. Both schemes are able to image the electrical properties of the subsurface. Relative performance of FEM and TEM systems is system dependent; however, the SkyTEM

system employed in this work is able to provide both shallow and deep information and has in general much larger depth of investigation compared to the FEM system. FEM systems' penetration depths are limited by the lowest available frequency. Operation at low frequencies reduces signal to noise ratios and can increase instrumentation weight (Steuer et al., 2009). Further, at great depth, the secondary magnetic field can be a small fraction of the primary magnetic field. Because FEM systems transmit and receive simultaneously, distinguishing the two fields can be difficult when the secondary field is weak; TEM systems sidestep this problem by measuring the secondary field when the primary field is off (zero) (Zhdanov, 2017).

TEM systems are particularly sensitive to conductive materials and can achieve maximum penetration (up to 400 - 600m in our survey) when conductive material is below resistive material. In this scenario, the deep conductive material generates a strong secondary magnetic field, and signal is not lost to attenuation within the resistive overburden. The collected TEM data were inverted using a spatially constrained inversion scheme (Auken and Christiansen, 2004; Viezzoli et al., 2008) in AarhusInv (Auken et al., 2014; Kirkegaard and Auken, 2015), which creates a quasi-3D resistivity model of the subsurface using a forward model that is based on 1D physics. Despite the 1D forward model, the spatially constrained inversion scheme imposes similarity amongst neighboring 1D models, allowing reproduction of 3D structures. In contrast to past results from the Dry Valleys that were collected using this SkyTEM system (Dugan et al., 2015; Mikucki et al., 2015; Foley et al., 2015), here we use a 'sharp' inversion, which prioritizes the production of models containing few layers of relatively homogenous intralayer properties (Vignoli et al., 2015). This results in sharp transitions between regions of contrasting resistivity, helping pinpoint horizons between neighboring layers. This inversion scheme is appropriate for the subsurface structure in our study region, which consists of high resistivity materials (glaciers, permafrost, sea ice) on top of conductive materials (saturated rock or sediments, saltwater lakes, seawater), where the strong geological stratification should coincide with similarly strong contrasts in electrical properties.

The presented inversion results are masked (i.e. not shown) beneath the depth of investigation (DOI) (Vest Christiansen and Auken, 2012). The DOI represents the depth to which the estimated resistivity profile has an appreciable impact on the data fit. Below the DOI, the estimated models cannot be discussed with great certainty as they are not well-constrained by the data. The DOI is reached within a few 10s of meters in seawater or highly conductive substrate but is 100s of meters deep when conductors lie beneath non-conductors, as in the case when permafrost or glaciers overlie saturated sediments. The reason for variable DOI is that the conductive seawater attenuates the TEM signal more rapidly (as a function of depth) than the non-conductive permafrost, thus allowing the system to image deeper when thick permafrost layers are present. More details on the system and processing for our Antarctic data are available in Foley et al (2015).

EM methods are useful in the cryosphere because changes in the phase of water (from liquid to solid) can correspond to orders of magnitude changes in electrical resistivity. TEM is well-suited to the targeted system in this work (permafrost overlying a conductive brine), in that the depth to the conductor can be well-constrained and the resistive overburden allows the system to penetrate deeper. Note that in regions of very thick permafrost or ice it can be difficult to generate a measurable signal, as the eddy currents produced in the resistive ice correspond to a very weak secondary field. As such, if the permafrost layer exceeds a certain thickness one can lose the ability to detect the presence of an underlying conductor. To

enhance depth penetration in these scenarios larger transmitter moments or lower internal noise receivers would be necessary.

Measuring Permafrost Thickness

Permafrost freezes from the top down which should be represented in EM-derived resistivities as a highly resistive (frozen) layer overlying a conductive (water saturated) layer. The measured bulk resistivity of this conductive layer depends on the resistivity of the fluid and the porosity of the material that contains the fluid. This can be estimated with an empirical relationship called Archie's Law:

$$\phi = \left(\frac{\rho_0}{\rho_b}\right)^{-1/m} \quad (1)$$

where ϕ is the porosity, ρ_0 is the bulk resistivity, $\rho_b$is the resistivity of the fluid and m is a 'formation factor' that represents the geometries of the pore network (Archie, 1950). Assuming that the fluids we measure have a resistivity similar to seawater, and assuming a moderate value for the formation factor, measured resistivities of 100 Ω-m and 10 Ω-m correspond to porosities of 6% and 19%, respectively. Despite the uncertainties in determining the porosity of a saturated sediment from resistivity alone, 100 Ω-m is a reasonable threshold to distinguish between permafrost and thawed material: it is too conductive to be permafrost or unweathered rock (Palacky, 1987), and has been shown to correspond to material transitions elsewhere in the region (Foley et al, 2015).

To estimate permafrost thickness, we determined the depth from the surface to the 100 Ω-m layer with the Aarhus Workbench software. Note that the depth to the permafrost/brine interface is well-resolved because of the strong resistivity contrast between these layers (and the thickness of the brine layer); significant changes to the estimated interface depth result in poorer data fits. We exclude any measurements acquired over the ocean, or, in limited cases, where the 100 Ω-m layer was not detected above the DOI.

Estimating Geothermal Flux

The simplest approach to estimating geothermal flux from permafrost thickness is to use (Osterkamp and Burn, 2003, based on their equation 1):

$$G \simeq K\frac{\Delta T}{Z} \quad (2)$$

where: G is the geothermal heat flux in SI units (W/m^2), K is the thermal conductivity of permafrost (W/m/C), and $\Delta T$is the temperature difference between the mean surface temperature and the freezing point at the bottom of the permafrost layer. Clearly, this simple equation is underlain by a number of assumptions. Firstly, this is a steady-state solution to a one-dimensional heat diffusion equation which implies that all of the quantities involved have not varied significantly over the period of time required to reach the steady state. A rough estimate of this equilibration time scale can be obtained by calculating the e-folding timescale, τ, for a one-dimensional heat diffusion problem for a layer of thickness Z:

$$\tau = \frac{Z^2}{D} \quad (3)$$

where D is the thermal diffusivity of the permafrost layer. In the absence of published values for thermal properties of phonolite, the primary rock in the study area, we use the diffusivity of 25.2 m^2/yr (8×10^{-7} m^2/s) for pure basalt (Hartlieb et al., 2015), the mineralogy of which has similar thermal properties (Horai and Simmons, 1969). We expect some interstitial ice in the permafrost layer; ice has a higher thermal diffusivity which would result in a shorter, hence less conservative, diffusive timescale. With the diffusivity of pure basalts, equation (3) yields an e-folding timescale of ~3,500 to ~6,500 years for Z of 300 to 400 m, as observed by us away from the coast (Figure 2). This period falls within the mid-to-late Holocene climate period during which long-term regional climate has been relatively stable, with a slight cooling of up to a few degrees towards the present time (Cunningham et al., 1999; Baggenstos et al., 2018). Hence, below we will assume that the permafrost thickness determined is in a steady state.

In the absence of surface temperature measurements from our study area, we use the standard (2 m above ground) mean annual temperature of -20°C from this region (Monaghan et al., 2005; Doran et al., 2002) plus an offset of +2°C to account for ground temperatures being a few degrees warmer in high polar regions than the corresponding mean annual temperature (e.g., Brown, 1966). This is consistent with surface temperatures projected from Dry Valleys Drilling Project (DVDP) borehole #3 on nearby Hut Point Peninsula (Decker and Bucher, 1982), a variety of temperature proxies from the McMurdo Sound Regions (Nichols and Ball, 1964) and observed mean annual air temperatures at McMurdo Station and Scott Base. For the temperature at the base of the permafrost we use the freezing point of seawater of ca. -1.9°C. We choose the freezing point of seawater rather than that of freshwater because we commonly observe very low electrical resistivities beneath the permafrost layer, e.g., ~10 Ω-m. Such bulk resistivity is difficult to obtain for freshwater saturated mafic rock, given that ~10 Ω-m is by itself a reasonable resistivity for groundwater. Using Archie's law (equation 1), this would imply that the material underneath the observed permafrost layer consists of unreasonably high fraction of groundwater. However, seawater has resistivity of 0.36 Ω-m and would yield bulk resistivity of saturated rock at sensible porosities of ca. 11-27% (Foley et al., 2015). The fact that our study area is in a coastal setting yields additional support to our assumption of seawater as the interstitial fluid beneath permafrost. With the mean annual surface temperature of -18°C and basal temperature of ca. -2°C, the temperature jump across the permafrost layer, ΔT, is ca. 16°C. This, together with permafrost thickness derived from our resistivity data allows us to calculate the geothermal gradient, which is then multiplied by thermal conductivity to obtain GHF. At low porosities thermal conductivity of basalts is slightly below 2 W/m/C while the thermal conductivity of ice itself is slightly higher than that (Horai, 1991). Here we use 2 W/m/C in our calculations of GHF, which is nearly the same as the thermal conductivity observed at the middle of DVDP borehole #3 at Hut Point Peninsula (Decker and Bucher, 1982), which has a similar geology to our study area.

The greatest limitation of the one-dimensional heat flow model (equation 2) is that it cannot account for the lateral heat flow from the ocean towards land (Risk and Hochstein, 1974). We use a two-dimensional finite difference heat conduction model to account for the impact of steady-state horizontal heat transfer from the seafloor towards land. The bespoke MATLAB code solves the standard two-dimensional heat diffusion equation (Recktenwald, 2004):

$$\frac{\partial T}{\partial t} = D\left(\frac{\partial^2 T}{\partial x^2} + \frac{\partial^2 T}{\partial z^2}\right) \quad (4)$$

where t is time and x, z are the two spatial coordinates and D has been assumed to be uniform throughout the subsurface domain. The seafloor is prescribed seawater temperature of -2°C while land surface temperatures are assigned using sea-level temperature of -18°C and a regional lapse rate of 0.0098 °C/m from Doran et al. (2002). The lower boundary condition is constant heat flux, equal to the prescribed geothermal flux, which is assumed to be constant across the lower boundary of the model domain. Both lateral boundaries are set to have zero horizontal heat flow. Initial conditions are given by temperatures following a linear vertical temperature gradient, equal to the assumed geothermal gradient, from the bottom of the domain to the land surface or seafloor.

The numerical solver uses the explicit forward time, centered space technique (Recktenwald, 2004). The code was verified by solving numerically a Dirichlet two-dimensional problem on a rectangle and then comparing the model output to an analytical harmonic solution. Although the code solves a transient partial differential equation (4) given above, we use it to approximate a steady-state solution by running it for long enough so that no element within the numerical domain changes its temperature by more than 10^{-6} °C per year. This typically happens after more than 20,000 model years of holding all boundary conditions constant.

RESULTS AND DISCUSSION

Analytical Results of Permafrost Thickness and Heat Flux

Using the 100 Ω-m layer as an indicator of unfrozen ground, we found the thickness of permafrost (or glacier ice, at Barne Glacier) across ~20 km^2 of the coastal western flank of Mt Erebus (Figure 2a). Permafrost is very thin at or near the coast and increases in thickness rapidly over the first ~500 m distance from the coast. Permafrost must necessarily be thin at the coast because the ocean is steady at about -1.9 °C, whereas mean annual air temperature at sea level is about -18 °C (Doran et al, 2002; Monaghan et al, 2004). This results in very high horizontal heat flow from the ocean to nearby land (including permafrost and glaciers).

The thin coastal permafrost is reflected in our derived analytical models. Given the low resistivity, we assume the base of the permafrost is at -1.9 °C (the freezing point of seawater) and the mean annual air temperature is -18 °C at sea level, with an environmental lapse rate of -6.5°C/km (Wallace and Hobbs, 2006). With these and the permafrost thickness, we calculate a vertical temperature gradient from bottom to top of the permafrost (Figure 2b). The temperature gradient is high near the coast due to the ocean's influence, but quickly settles to ~45 °C/km inland. To estimate the uncertainty on this geothermal gradient, we use the square-root-of-the-sum-of-squares assuming ~10% standard deviation on ΔT (ca. ±1.6 °C) and 5% standard deviation on Z (ca. ±20m for a 400m-thick layer). This estimate yields one standard deviation of 11%, which for the geothermal gradient of ~45 °C/km is ±5 °C/km.

We estimate vertical heat flux (Figure 2c) by assuming a thermal conductivity for basaltic material with ice filling its pores of 2.0 W/m C (based on Horai, 1991). The vertical heat flux is very high (>300 mW/m^2) near the coast, but settles to ~90 mW/m^2 inland, which is slightly high for the global average but reasonable for the region, which has high geothermal flux (Decker and Bucher, 1982), especially given the site's location on the flank of Mt Erebus, an active volcano, and in an area of regional extension. We add an estimated uncertainty in thermal conductivity of basaltic material of 10% (i.e., one standard deviation of ±2 mW/m^2) to the uncertainty in geothermal gradient calculated above to arrive at one standard deviation for GHF of 15%, i.e., about ±13 mW/m^2 for ~90 mW/m^2.

Past measurements of temperature gradient and heat flux from boreholes on Ross Island have noted the importance of heat flow from the ocean (Risk and Hochstein, 1974). Even accounting for the ocean's influence, heat flow is variable in this region. Risk and Hochstein (1974) measured fluxes of 164 $mW/m^2 \pm 60$ mW/m^2 at Arrival Heights on Hut Point Peninsula (near McMurdo Station, see Fig. 1), which they attributed to recent volcanic activity on the peninsula. Our data come from an old part of the volcano with a complicated history of subsequent eruptive and intrusive events (Esser et al, 2004). Because our technique does not directly measure heat flux, but rather derives it from its effect on permafrost thickness, it may integrate heat sourced from older and more recent volcanic events, and thus be less biased by recent events, than a single borehole measurement could be.

Our two-dimensional numerical heat flow model includes the effect of lateral heat transfer from the ocean on subsurface temperature distribution and calculated permafrost thickness (Figure 3a). Comparison of the permafrost thickness distribution derived from resistivity observations with the permafrost thickness predicted by the model shows, however, a significant mismatch (Figure 3b). The model predicts that the excess vertical heat flux caused by the heat exchange between land and the ocean should decay relatively rapidly inland, within a distance equal to about one to two permafrost thicknesses (Figure 3c). Beyond this distance the impact of conductive heat transfer between the land and ocean domains should be quite small. In our model, this leads to a very rapid rise of the permafrost thickness near the coastline so that the simulated permafrost thickness reaches half of its 'inland' value within just a few hundred meters from the coast. In contrast, the permafrost thickness based on the 100 Ω-m resistivity threshold rises only slowly over the first several hundred meters and then more rapidly further from the coast. We concur with the suggestion of Risk and Hochstein (1974) that near-shore permafrost on Ross Island, and perhaps in general, may be subject to seawater intrusion. As seawater intrudes into colder permafrost it may become cryoconcentrated into hypersaline brine, leading to development of a 'slushy' permafrost zone whose bulk resistivity drops below the 100 Ω-m threshold used here to define frozen ground.

CONCLUSIONS

While direct measurements of such fundamental geologic and geophysical properties like geothermal heat flux, groundwater salinity, and permafrost are desirable, practical or environmental considerations often render them unattainable in many polar locations. In a span of one day we collected EM resistivity data that allowed us to infer some of these properties and achieve results consistent with past measurements within the region. We estimate that the permafrost layer (here defined as near-surface material with bulk resistivity >100 Ω-m) is 300-400m thick in the region, except in the near-shore environment where it rapidly decays to nil at the coastline. This decay is partly due to lateral conductive heat flux from the warm ocean to the cold adjacent land. We also speculate that intrusion of seawater into coastal permafrost further impacts the properties of the nearshore permafrost, likely making it <100 Ω-m in resistivity. Our resistivity data do not suggest any positive evidence for local hydrothermal circulation (e.g., localized thinning of the permafrost layer) and do not necessitate invoking geologic control on subsurface resistivity distribution on the flank of this active volcano. Based on relatively low resistivities of the sub-permafrost material, we speculate that basaltic rocks are saturated by seawater in this coastal zone. The estimated geothermal gradient away from the coast is about 45 °C/km ±5 °C/km and geothermal flux ca. 90 mW/m^2 ±13 mW/m^2. These values are close to the middle of the range for other

measurements of geothermal gradient and geothermal flux in this region (e.g., Morin et al., 2010).

ACKNOWLEDGEMENTS

This material is based upon work supported by the National Science Foundation under grant no. 1344349 to S. Tulaczyk and 1241503, and 1344348 to J. Mikucki. Invaluable field support was provided by Raytheon Polar Services and the PHI helicopter pilots. The initial idea for this survey and manuscript originated with Prof. Phil Kyle, to whom we are deeply grateful for the inspiration.

FIGURES

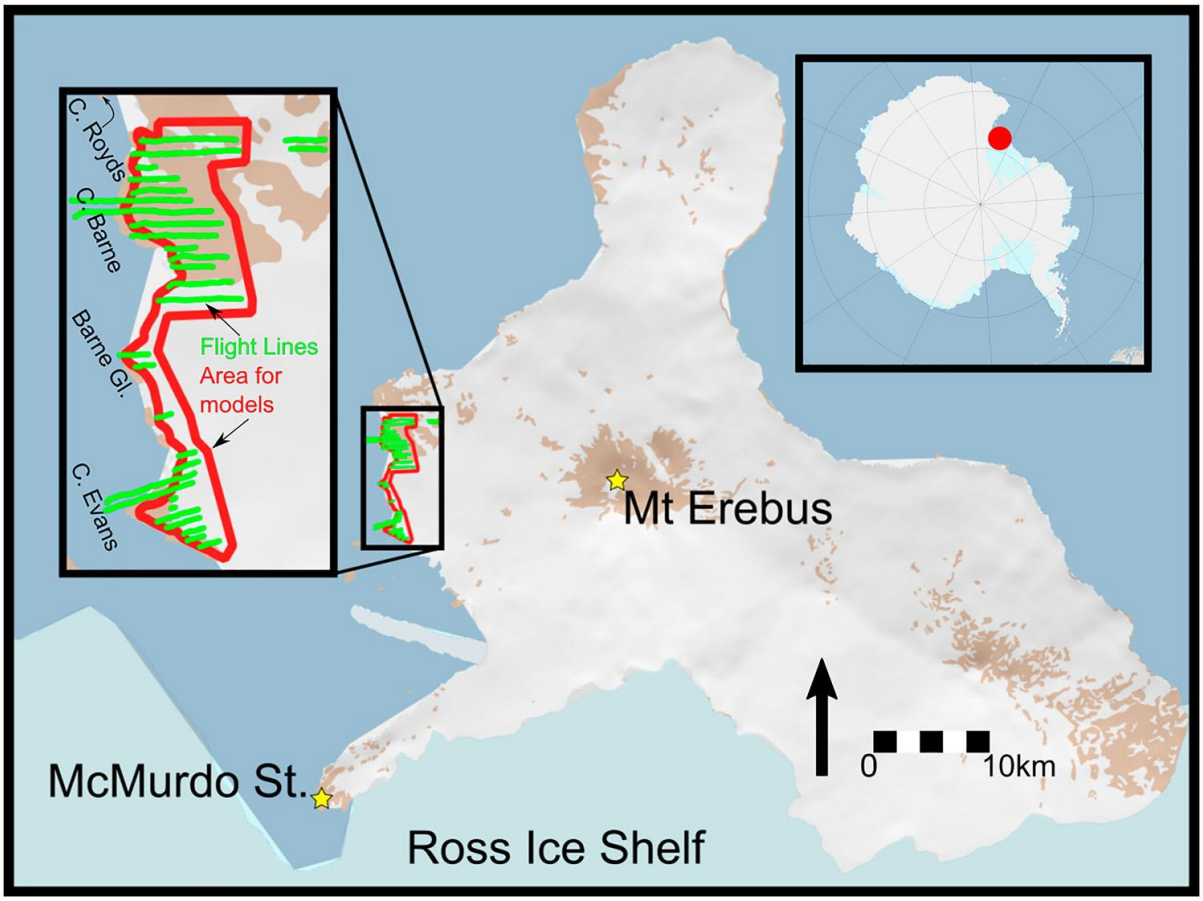

Fig. 1: Map of the field area. Ross Island is depicted in the main figure frame and the inset shows the location of survey flightlines in green. The northern flightlines cover the southern edge of Cape Royds & Cape Barne and the southern flightlines cover Cape Evans. In between, a few short lines cover the terminus of the Barne Glacier. The red outline marks the extent of data displayed in Figure 2. Measurements outside the red outline were either over water (limited DOI) or high residual, low signal measurements that were too far from the bulk of the data to use in our calculations.

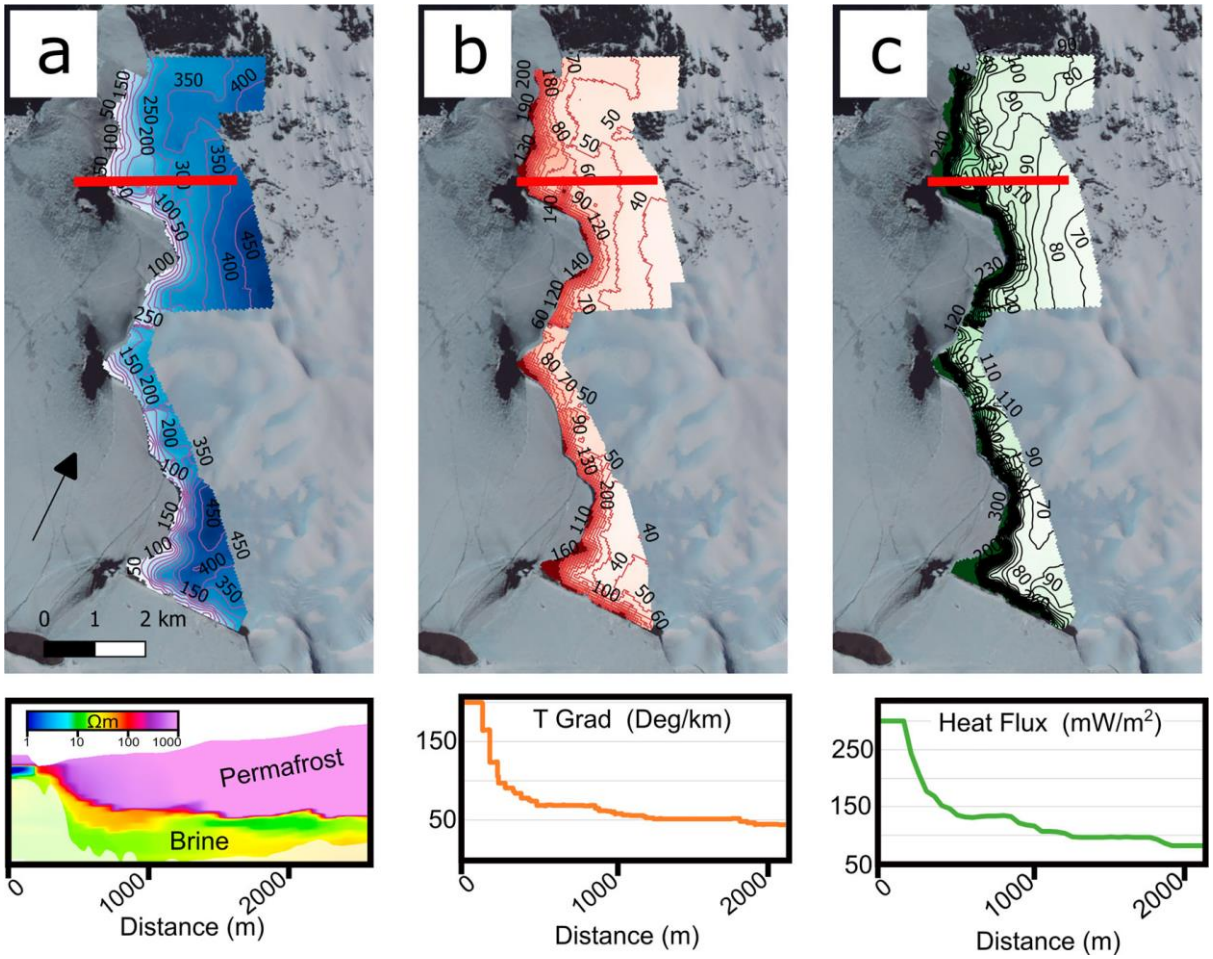

Fig 2. Results and calculations derived from EM measurements. In each, a cross section is shown along the same red line marked on the map. (a) Permafrost thickness, as calculated by depth from the surface to the 100 Ω-m layer. Contours are in 50m increments. Permafrost is very thin near the coast and increases in thickness more gradually inland. The cross section shows a profile through the resistivity data that were used to calculate permafrost thickness. The resistivity results are faded below the DOI. (b) The vertical temperature gradient from the bottom of the permafrost to the top. Contours are in 10 °C/km increments. Values are capped at 200 °C/km (near the ocean, where the permafrost is thin). (c) Vertical heat flux (mW/m^2) through the permafrost. Contours are in 10 mW/m^2 increments. Capped at 300 mW/m^2 near the coast where permafrost is thin.

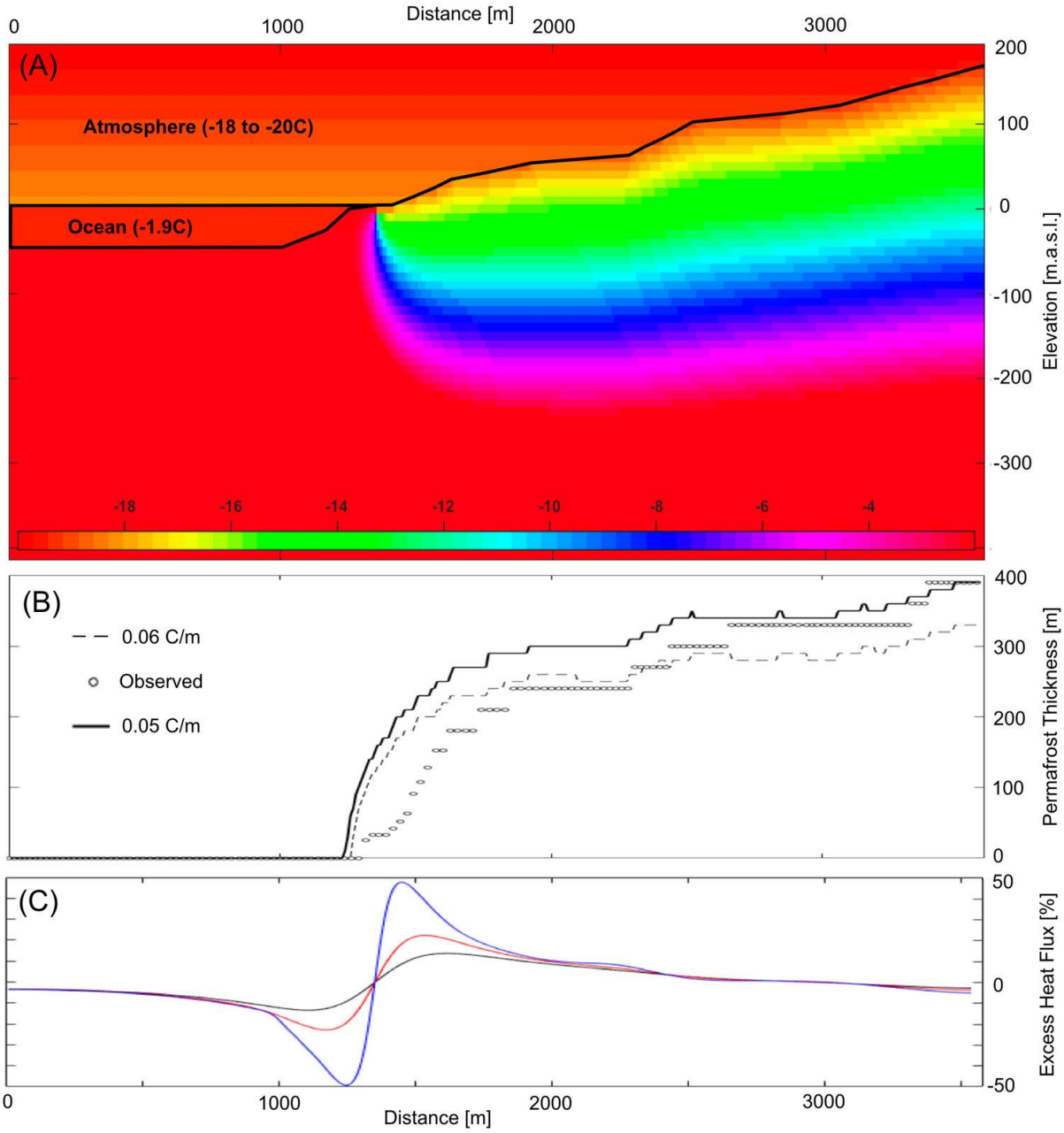

Fig 3. Temperature field from a two-dimensional heat flow model (a). The scale is chosen to show only the temperature range within the permafrost layer. Surface topography and the position of the coastline are taken from the same profile line shown above in Figure 2. This example is for assumed geothermal gradient of 60 °C/km. In panel (b) we show a comparison between the permafrost thickness distribution based on resistivity data (circles) and simulated permafrost thickness for two different values of geothermal gradient: 60 °C/km in dashed line and 50 °C/km in solid line. The lowermost pane (c) illustrates the high magnitude of excess vertical heat flux near the coastline. The excess vertical heat flux (in %) is calculated by subtracting the prescribed geothermal heat flux from the total vertical heat flow and then dividing the difference by the prescribed geothermal heat flux. The blue line shows the distribution at 100m below sea level, the red line at 200m below sea level and the black line at 300m below sea level.

REFERENCES

Archie, G. E. 1950. Introduction to petrophysics of reservoir rocks. AAPG Bulletin 34, 943–961.
Auken, E., and A.V. Christiansen. 2004. Layered and laterally constrained 2D inversion of resistivity data. Geophysics 69, no. 3: 752–61. https://doi.org/10.1190/1.1759461.

Auken, E., A.V. Christiansen, C. Kirkegaard, G. Fiandaca, C. Schamper, A.A. Behroozmand, A. Binley, et al. 2015. An overview of a highly versatile forward and stable inverse algorithm for airborne, ground-based and borehole electromagnetic and electric data. Exploration Geophysics 46, no. 3: 223–35. https://doi.org/10.1071/EG13097.

Baggenstos, D., J.P. Severinghaus, R. Mulvaney, J.R. McConnell, M. Sigl, O. Maselli, J.R. Petit, B. Grente, and E.J. Steig. 2018. A horizontal ice core from Taylor glacier, its implications for Antarctic climate history, and an improved Taylor Dome ice core time scale. Paleoceanography and Paleoclimatology 33: 778–94.

Ball, L.B., B.D. Smith, B.J. Minsley, J.D. Abraham, C.I. Voss, M. Deszcz-Pan, and J.C. Cannia. 2011. Airborne electromagnetic and magnetic survey data of the Yukon Flats and Ft. Wainwright areas, central Alaska, June 2010, U.S. Geol. Surv. Open File Rep., 2011–1304, 28 pp.

Begeman, C.B., S.M. Tulaczyk, and A.T. Fisher. 2017. Spatially variable geothermal heat flux in West Antarctica: Evidence and implications. Geophysical Research Letters 44, no. 19: 9823–32.

Bentley, C. R. 1977. Electrical Resistivity Measurements On The Ross Ice Shelf. Journal of Glaciology 18, 15–35.

Brown, R.J.E. 1966. Relation between mean annual air and ground temperatures in the permafrost region of Canada. In Proceedings of the permafrost international conference: Proceedings, NAS-NRC Publication No. 1287, 241–6.

Christiansen, A.V., and E. Auken. 2012. A global measure for depth of investigation. Geophysics 77, no. 4: WB171–7. https://doi.org/10.1190/geo2011-0393.1.

Cunningham, W.L., A. Leventer, J.T. Andrews, A.E. Jennings, and K.J. Licht. 1999. Late Pleistocene-Holocene marine conditions in the Ross Sea, Antarctica: evidence from the diatom record. The Holocene 9, no. 2: 129–39.

Davies, J.H., and D.R. Davies. 2010. Earth's surface heat flux. Solid Earth 1, no. 1: 5–24.

Decker, E., and G. Bucher. 1982. Geothermal studies in the Ross Island-Dry Valley region. International Union of Geological Sciences, Ser. B.

Doran, P.T., C.P. McKay, G.D. Clow, G.L. Dana, A.G. Fountain, T. Nylen, and W.B. Lyons. 2002. Valley floor climate observations from the McMurdo Dry Valleys, Antarctica, 1986–2000. Journal of Geophysical Research: Atmospheres 107, no. D24: ACL-13.

Doran, P.T., and W.F. Vincent. 2011. Environmental protection and stewardship of subglacial aquatic environments. In Antarctic subglacial aquatic environments, Vol. 192, 149–57. Washington, DC: American Geophysical Union.

Dugan, H.A., P.T. Doran, S. Tulaczyk, J.A. Mikucki, S.A. Arcone, E. Auken, C. Schamper, and R.A. Virginia. 2015. Subsurface imaging reveals a confined aquifer beneath an ice-sealed Antarctic lake. Geophysical Research Letters 42, no. 1: 96–103. doi.org/10.1002/2014GL062431.

Esser, R.P., P.R. Kyle, and W.C. McIntosh, McIntosh William C. 2004. 40Ar/39Ar dating of the eruptive history of Mount Erebus, Antarctica: Volcano evolution. Bulletin of Volcanology 66: 671–86. https://doi.org/10.1007/s00445-004-0354-x.

Fisher, A.T., K.D. Mankoff, S.M. Tulaczyk, S.W. Tyler, and N. Foley. 2015. High geothermal heat flux measured below the West Antarctic Ice sheet. Science Advances 1, no. 6: e1500093.

Foley, N., S. Tulaczyk, E. Auken, C. Schamper, H. Dugan, J. Mikucki, R. Virginia, and P. Doran. 2015. Helicopter-borne transient electromagnetics in high-latitude environments: An application in the McMurdo Dry Valleys, Antarctica. Geophysics 81: WA87–99. doi:10.1190/geo2015-0186.1.

Foley, N., S.M. Tulaczyk, D. Grombacher, P.T. Doran, J. Mikucki, K.F. Myers, et al. 2019. Evidence for pathways of concentrated submarine groundwater discharge in East Antarctica from helicopter-borne electrical resistivity measurements. Hydrology 6, no. 2: 54. https://doi.org/10.3390/hydrology6020054.

Haas, C., J. Lobach, S. Hendricks, L. Rabenstein, and A. Pfaffling. 2009. Helicopter-borne measurements of sea ice thickness, using a small and lightweight, digital EM system. Journal of Applied Geophysics 67: 234–41.

Harpel, C.J., P.R. Kyle, R.P. Esser, W.C. McIntosh, and D.A. Caldwell. 2004. 40Ar/39Ar dating of the eruptive history of Mount Erebus, Antarctica: Summit flows, tephra, and caldera collapse. Bulletin of Volcanology 66, no. 8: 687–702.

Hartlieb, P., M. Toifl, F. Kuchar, R. Meisels, and T. Antretter. 2016. Thermo-physical properties of selected hard rocks and their relation to microwave-assisted comminution. Minerals Engineering 91: 34–41.

Hauck, C., M. Guglielmin, K. Isaksen, and D. Vonder Mühll. 2001. Applicability of frequency-domain and time-domain electromagnetic methods for mountain permafrost studies. Permafrost and Periglacial Processes 12, no. 1: 39–52. https://doi.org/10.1002/ppp.383.

Hill, G., P.E. Wannamaker, J.A. Stodt, M.J. Unsworth, V. Maris, P. Bedrosian, E. Wallin, et al. 2017. Imaging the magmatic system of Erebus volcano, Antarctica using the magnetotelluric method. In American Geophysical Union, Fall Meeting 2017, abstract #T22D-08. Retrieved from http://adsabs.harvard.edu/abs/2017AGUFM.T22D..08H.

Hochstein, M. 1967. Electrical Resistivity Measurements on Ice Sheets. Journal of Glaciology 6, 623–633.

Horai, K. 1991. Thermal conductivity of Hawaiian basalt: A new interpretation of Robertson and Peck's data. Journal of Geophysical Research: Solid Earth. 96 (B3): 4125–32. doi:10.1029/90JB02452.

Horai, K., and G. Simmons. 1969. Thermal conductivity of rock-forming minerals. Earth and Planetary Science Letters 6, no. 5: 359–68. https://doi.org/10.1016/0012-821X(69)90186-1.

Kirkegaard, C., and E. Auken. 2015. A parallel, scalable and memory efficient inversion code for very large-scale airborne electromagnetics surveys. Geophysical Prospecting 63, no. 2: 495–507. https://doi.org/10.1111/1365-2478.12200.

Kirsch, R. 2009. Groundwater geophysics – A tool for hydrogeology. 2nd ed. Berlin: Springer-Verlag.

Korhonen, K., T. Ruskeeniemi, M. Paananen, and J. Lehtimäki. 2009. Frequency domain electromagnetic soundings of Canadian deep permafrost. Geophysica 45, no. 1–2: 77–92.

Kovacs, A., and J.S. Holladay. 1990. Sea-ice thickness measurement using a small airborne electromagnetic sounding system. Geophysics 55, no. 10: 1327–37.

Kyle, P.R. 1990. Geothermal resources of Antarctica. Mineral Resources Potential of Antarctica 51: 117–23.

Lachenbruch, A.H., J.H. Sass, B.V. Marshall, and T.H. Moses Jr. 1982. Permafrost, heat flow, and the geothermal regime at Prudhoe Bay, Alaska. Journal of Geophysical Research: Solid Earth 87, no. B11: 9301–16.

McGinnis, L. D., K. Nakao, and C. C. Clark. 1973. Geophysical Identification of Frozen and Unfrozen Ground Antarctica: Permafrost North American Contribution Second International Conference, 136–146.

McKenzie, J.M., and C.I. Voss. 2013. Permafrost thaw in a nested groundwater-flow system. Hydrogeology Journal 21, no. 1: 299–316.

Melles, M., J. Brigham-Grette, P. Minyuk, C. Koeberl, A. Andreev, T. Cook, G. Fedorov, et al. 2011. The Lake El'gygytgyn scientific drilling project–conquering arctic challenges through continental drilling. Scientific Drilling 11: 29–40.

Mikucki, J.A., E. Auken, S. Tulaczyk, R.A. Virginia, C. Schamper, K.I. Sørensen, P.T. Doran, H. Dugan, and N. Foley. 2015. Deep groundwater and potential subsurface habitats beneath an Antarctic dry valley. Nature Communications 6: 6831. doi:10.1038/ncomms7831.

Minsley, B.J., J.D. Abraham, B.D. Smith, J.C. Cannia, C.I. Voss, M.T. Jorgenson, M.A. Walvoord, et al. 2012. Airborne electromagnetic imaging of discontinuous permafrost. Geophysical Research Letters 39, no. 2. https://doi.org/10.1029/2011GL050079.

Monaghan, A.J., D.H. Bromwich, J.G. Powers, and K.W. Manning. 2005. The climate of the McMurdo, Antarctica, region as represented by one year of forecasts from the Antarctic mesoscale prediction system. Journal of Climate 18, no. 8: 1174–89.

Morin, R.H., T. Williams, S.A. Henrys, D. Magens, F. Niessen, and D. Hansaraj. 2010. Heat flow and hydrologic characteristics at the AND-1B borehole, ANDRILL McMurdo Ice Shelf Project, Antarctica. Geosphere 6, no. 4: 370–8.

Multala, J., H. Hautaniemi, M. Oksama, M. Lepparanta, J. Haapala, A. Herlevi, K. Riska, and M. Lensu. 1996. An airborne electromagnetic system on a fixed wing aircraft for sea ice thickness mapping. Cold Regions Science and Technology 24, no. 4: 355–73.

Nichols, R. L., and D. G. Ball. 1964. Four-fold check on mean annual temperature, McMurdo Sound, Antarctica. Journal of Glaciology 5, 353–355.

Osterkamp, T.E., and C.R. Burn. 2003. Permafrost. In Encyclopedia of atmospheric sciences, ed. J.R. Holton, J.Pyle, and J.A. Curry, 1717–29. Oxford, UK: Academic Press.

Palacky, G.V. 1987. Resistivity characteristics of geologic targets. Electromagnetic Methods in Applied Geophysics 1 (Theory): 1351.

Parmelee, D.E., P.R. Kyle, M.D. Kurz, S.M. Marrero, and F.M. Phillips. 2015. A new Holocene eruptive history of Erebus volcano, Antarctica using cosmogenic 3He and 36Cl exposure ages. Quaternary Geochronology 30: 114–31.

Pfaffling, A., C. Haas, and J.E. Reid. 2007. Direct helicopter EM—Sea-ice thickness inversion assessed with synthetic and field data. Geophysics 72, no. 4: F127–37. https://doi.org/10.1190/1.2732551.

Rack, W., C. Haas, and P.J. Langhorne. 2013. Airborne thickness and freeboard measurements over the McMurdo Ice Shelf, Antarctica, and implications for ice density. Journal of Geophysical Research: Oceans 118, no. 11: 5899–907. https://doi.org/10.1002/2013JC009084.

Ragnarsson, Á. 2003. Utilization of geothermal energy in Iceland. In International geothermal conference, Reykjavik, September 2003, paper 123, 39–45.

Recktenwald, G.W. 2004. Finite-difference approximations to the heat equation. Mechanical Engineering 10: 1–27.

Risk, G.F., and M.P. Hochstein. 1974. Heat flow at arrival heights, Ross Island, Antarctica. New Zealand Journal of Geology and Geophysics 17, no. 3: 629–44.

Ruotoistenmäki, T., and J. Lehtimäki. 1997. Estimation of permafrost thickness using ground geophysical measurements, and its usage for defining vertical temperature variations in continental ice and underlying bedrock. Journal of Glaciology 43, 359–364.

Sørensen, K.I., and E. Auken. 2004. SkyTEM–A new high-resolution helicopter transient electromagnetic system. Exploration Geophysics 35, no. 3: 194–202.

Steuer, A., B. Siemon, and E. Auken. 2009. A comparison of helicopter-borne electromagnetics in frequency- and time-domain at the Cuxhaven valley in Northern Germany. Journal of Applied Geophysics 67, no. 3: 194–205. https://doi.org/10.1016/j.jappgeo.2007.07.001.

Todd, B.J., and S.R. Dallimore. 1998. Electromagnetic and geological transect across permafrost terrain, Mackenzie River delta, Canada. Geophysics 63, no. 6: 1914–24. https://doi.org/10.1190/1.1444484.

Todd, B.J., and S.R. Dallimore. 2002. Electromagnetic and geological transect across permafrost terrain, Mackenzie River delta, Canada. Geophysics 63, 1914–24.

Tulaczyk, S., J.A. Mikucki, M.R. Siegfried, J.C. Priscu, C.G. Barcheck, L.H. Beem, A. Behar, et al. 2014. WISSARD at Subglacial Lake Whillans, West Antarctica: scientific operations and initial observations. Annals of Glaciology 55, no. 65: 51–8.

Viezzoli, A., A.V. Christiansen, E. Auken, and K. Sørensen. 2008. Quasi-3D modeling of airborne TEM data by spatially constrained inversion. Geophysics 73, no. 3: F105–13.

Vignoli, G., G. Fiandaca, A.V. Christiansen, C. Kirkegaard, and E. Auken. 2015. Sharp spatially constrained inversion with applications to transient electromagnetic data. Geophysical Prospecting 63, no. 1: 243–55.

Wallace, J., and P. Hobbs. 2006. Atmospheric science: An introductory survey. 483 pp. Burlington, Mass: Academic Press.

Wannamaker, P. E., J. A. Stodt, L. Pellerin, S. L. Olsen, and D. B. Hall. 2004. Structure and thermal regime beneath the South Pole region, East Antarctica, from magnetotelluric measurements. Geophysical Journal International 157, 36–54.

Wannamaker, P., G. Hill, J. Stodt, V. Maris, Y. Ogawa, K. Selway, G. Boren, E. Bertrand, D. Uhlmann, B. Ayling, A. M. Green, and D. Feucht. 2017. Uplift of the central transantarctic mountains. Nature Communications 8, 1588.

Worby, A., P. Griffin, V. Lytle, and R. Massom. 1999. On the use of electromagnetic induction sounding to determine winter and spring sea ice thickness in the Antarctic. Cold Regions Science and Technology 29, no. 1: 49–58. https://doi.org/10.1016/S0165-232X(99)00003-8.

Zhdanov, S.M. 2017. Airborne electromagnetic methods. In Foundations of geophysical electromagnetic theory and methods, 663–81. Elsevier. https://doi.org/10.1016/b978-0-44-463890-8.00020-7.